HOSTED BY

ELSEVIER

Available online at www.sciencedirect.com

ScienceDirect

Journal of Magnesium and Alloys 4 (2016) 44–51
www.elsevier.com/journals/journal-of-magnesium-and-alloys/2213-9567

Full Length Article

Effect of yttrium on corrosion behavior of extruded AZ61 Mg alloy

Li Li [a,b,*], Nguyen Dang Nam [b]

[a] *Institute of Advanced Manufacturing Technology, Hunan Institute of Technology, Hengyang, Hunan Province 421002, China*
[b] *Institute for Frontier Materials, Deakin University, Geelong Waurn Ponds Campus, Victoria 3220, Australia*

Received 22 August 2015; revised 29 November 2015; accepted 30 November 2015

Available online 29 January 2016

Abstract

The corrosion behavior of extruded AZ61 magnesium alloy with different addition of yttrium ranging from 0 to 0.9 wt. % was investigated. The electrochemical techniques in naturally-aerated 0.01 M NaCl solution and the surface analyses are utilized. The electrochemical results show that the pitting potential, time to pitting initiation, film and charge transfer resistances of the AZ61 specimens increased with the increase of yttrium content. Surface analyses indicate that yttrium promotes the formation of passive films and the refinement of the precipitates and matrix grains.

Keyword: Magnesium alloy; Polarization; Alkaline corrosion; Pitting corrosion

1. Introduction

Wrought magnesium alloys have great potential applications in the automotive industry due to the interest in using light-weight magnesium as automotive sheet and extrusion for vehicle body applications [1], but still their corrosion resistance and formability are quite questionable [2]. Therefore, the corrosion resistance of magnesium and its alloys attract more and more attentions and should be improved to achieve the required corrosion resistance for the industries.

Recently, the corrosion resistance of magnesium alloys has been improved by optimizing its microstructure [3], adding certain alloying elements [4], adopting appropriate surface treatments [5], and controlling texture [6]. In fact, many reports have pointed out that galvanic corrosion processes [7] are significant concerns for engineering applications of the alloys. It has been reported [8] that not only the mechanical properties but also the corrosion resistance of Mg alloys vary significantly with the introduction of rare earth alloying elements. The improvement could be attributed to the suppression of the micro-galvanic couples due to decrease in the fraction of β phases ($Mg_{17}Al_{12}$) and the deposited rare earth-containing phases to be less cathodic [9]. The beneficial effects of rare earth elements on corrosion properties of magnesium alloys can be attributed to the effect of passive cathode [2], the carbonates on the corrosion film [10] and scavenger [11]. Recently, it has been reported that the hot deformation improved the mechanical properties and cause significant changes in the microstructure of Mg alloys [12,13]. The addition of yttrium (Y) and other rare earth elements remarkably improves the corrosion resistance of magnesium alloys for the promotion of passive film formation, refinement of the precipitates and grain size. Moreover, the standard electrochemical potential of Y is close and seems to be equal to Mg [14]. Kashefi et al. [15] also reported that AZ80—1.0Y exhibited a better creep behavior due to a higher volume fraction of thermally stable Al_2Y and lower amounts of less stable $Mg_{17}Al_{12}$. This suggests that Y has been strongly recommended as an alloying element to improve the corrosion behavior of AZ61 alloy. Thus, we investigate the corrosion property of AZ61 alloys containing yttrium using electrochemical and surface characterization methods.

2. Experimental

2.1. Specimen preparation

The as-cast ingots of AZ61—xY (x = 0.0, 0.2, and 0.9 wt. %) alloy were homogenized at 520 °C for 8 hours with subsequent cooling in air. The researched alloy was extruded at 375 °C using an extrusion ratio of 16:1 and a constant RAM speed of 2 mm/min. The specimens used for corrosion tests were cut from the extruded rods along the direction normal to

* Corresponding author. Institute of Advanced Manufacturing Technology, Hunan Institute of Technology, Hengyang, Hunan Province 421002, China. Tel.: +86 0734 3452206; fax: +86 7343452206. Li, Ph.D., and Nam, Ph.D., contributed equally to this work. The research was financially supported by Scientific Research Project of Hunan Institute of Technology (HGLX001).

E-mail address: lileewin@163.com (L. Li).

http://dx.doi.org/10.1016/j.jma.2015.11.008
2213-9567/

extrusion axis. For the observation of the microstructure, the extruded specimens were finished by grinding with 1200-grit, 4000-grit silicon carbide paper and then 0.5 μm diamond powders. These specimens were etched by acetic acid (10 ml) + picric acid (5 g) + ethanol (70 ml of 95% purity) + distilled water (10 ml).

2.2. Electrochemical investigation methods

The electrochemical experiments were conducted at room temperature in naturally-aerated 0.01 M NaCl solution 0.01 M NaCl solution (pH = 12) with the exposure area of 78.5 mm^2. Potentiodynamic polarization and potentiostatic tests were performed using a VSP system (Biologic Scientific Instruments). A large surface area of titanium mesh counter electrode and a silver/silver chloride (Ag/AgCl) reference electrode were adopted. In order to stabilize the open-circuit potential, the samples were immersed in the solution for 1 hour before the potentiodynamic polarization test. The potential of the electrodes was scanned at a rate 0.166 mV/s ranging from −250 mV versus Ecorr to 300 mVAg/AgCl. The electrochemical impedance spectroscopy (EIS) was conducted at OCP with a peak-to-peak amplitude of the sinusoidal perturbation of 10 mV and the frequency ranging from 100 kHz to 10 MHz. Tests were conducted for every 1 hour over a period of 10 hours.

2.3. Surface analyses

To highlight the surface morphology of pitting, the specimens were examined by scanning electron microscopy (SEM/EDS) after pitting initiation. The corresponding microstructures were observed by scanning electron microscopy (SEM) after etching. The constituent phases of the as-received specimens were finished by XRD using Cu Kα radiation.

3. Results

3.1. Alloy microstructure and composition

The microstructures of the AZ61 alloys with different amounts of Y addition are shown in Fig. 1. The microstructures consist of α-Mg matrix and precipitates, whose sizes and distribution are very different among three type alloys, respectively. It also shown that the large particles were located on the grain boundary and within α-Mg matrix of the AZ61 and AZ61—0.2Y alloy specimens, while the smaller and uniform particles were observed in AZ61—0.9Y structure. The results analyzed by SEM/EDS clearly show that rich in Al and Zn elements were located on the grain boundary in the AZ61 specimens, whereas the particles rich in Al, Zn and Y in AZ61 + 0.2Y specimens as shown in Fig. 2b.

The phase constitutes of the AZ61—xY specimens were also identified by XRD and their patterns are presented in Fig. 3. The obvious differences exist in the α-Mg peaks between the AZ61 and Y-containing specimens. XRD results also indicate the peaks of Mg and $Mg_{17}Al_{12}$ with an additional peak close to the reflections by $Al_{11}Y_3$ obtained in Y-containing specimens. An increase in the intensity from α-Mg and $Al_{11}Y_3$ peaks could be attributed to the reaction of Y with Al to produce Al—Y phase. This is due to large difference in the electronegativity between

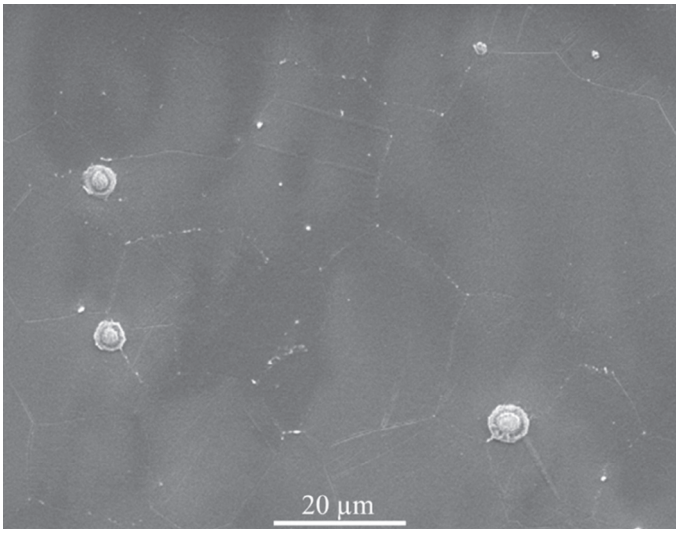

(a)

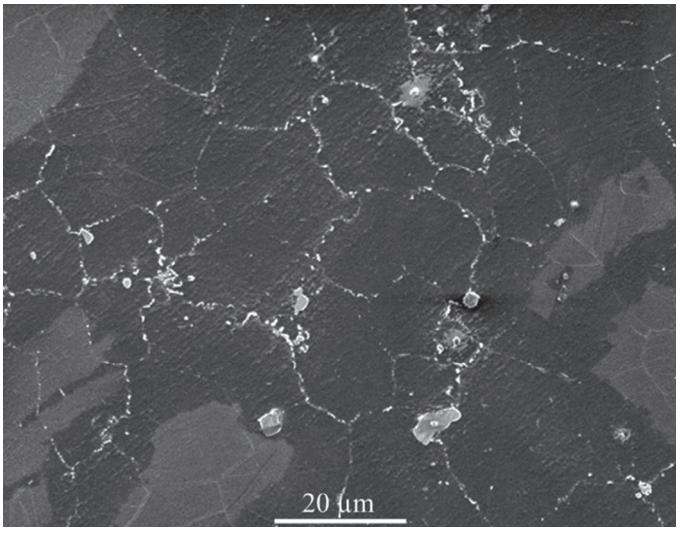

(b)

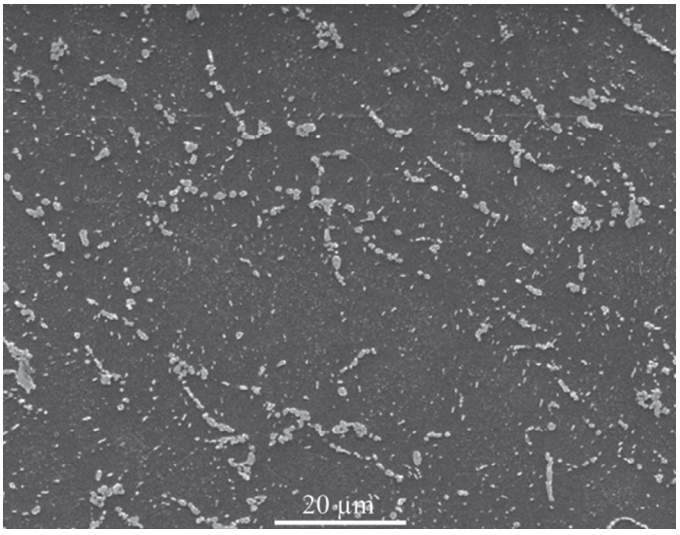

(c)

Fig. 1. SEM micrographs: (a) AZ61, (b) 0.2Y, and (c) 0.9Y addition.

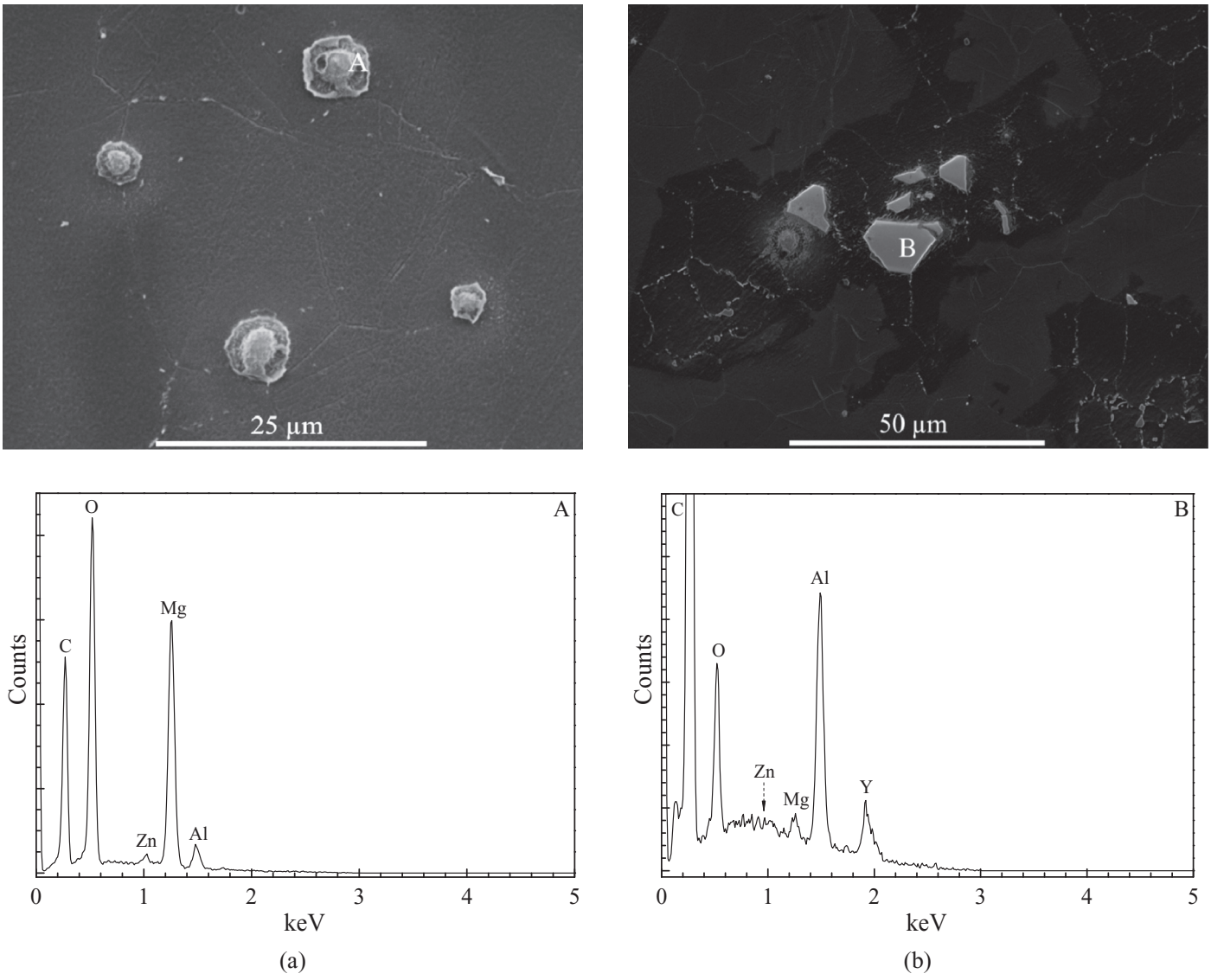

Fig. 2. SEM image and EDS spectrum of the intermetallic particles in (a) AZ61 and (b) 0.2Y-containing specimens.

Y and Al when compared to Y and Mg. A decrease in the resultant amount of β-$Mg_{17}Al_{12}$ is expected in the Y-containing specimens because part of the Al reacts with Y to form the intermetallic compounds i.e. $Al_{11}Y_3$. Al—Y phases were observed in all the Y-containing specimens and increased with the increase of Y content. Noting the strong signal of O and Zn were collected in the EDS spectrum Fig. 2, the Zn elements probably exist in the form of zinc oxide. The strong diffraction peaks of zinc oxide are coincident with α-Mg [16], so it cannot be distinguished from the XDR patterns in Fig. 3.

It could be concluded that the microstructure is the primary α grains surrounded by a eutectic mixture of α and precipitates. The specimen had relatively small α-Mg grains, which contained more precipitates at both grain boundary and α-Mg matrix with the increase of Y content. Furthermore, the distribution of precipitates became more uniform in the specimens with the increase of Y content. It could influence the corrosion performance due to smaller grain size, higher precipitation

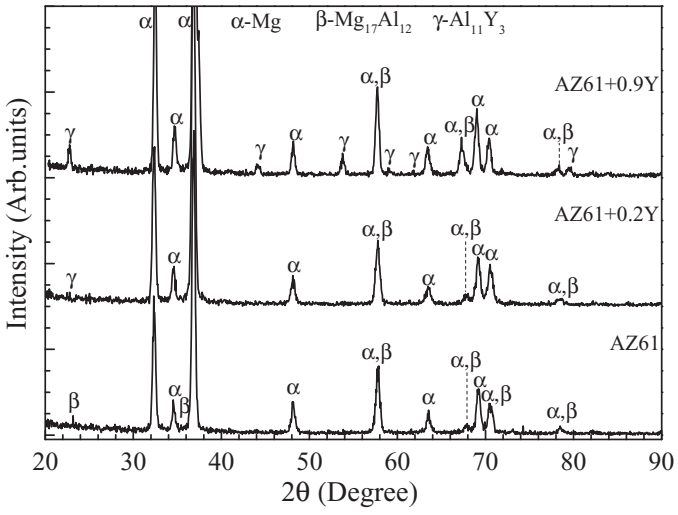

Fig. 3. XRD patterns of various AZ61 alloys.

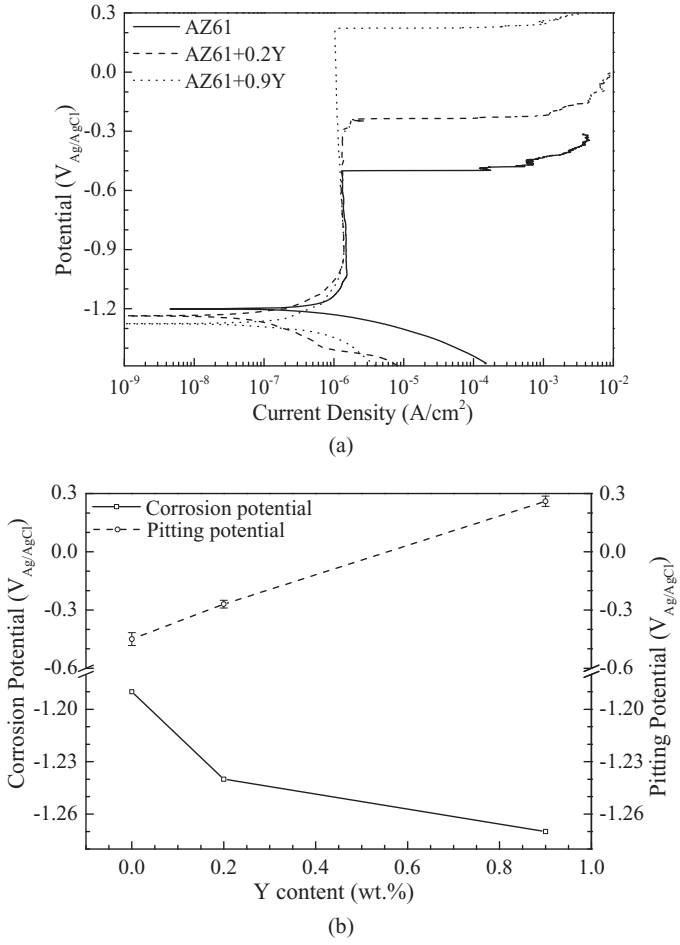

Fig. 4. (a) Potentiodynamic polarization curves of AZ61 as a function of Y content and (b) effect of Y on corrosion and pitting potentials of AZ61.

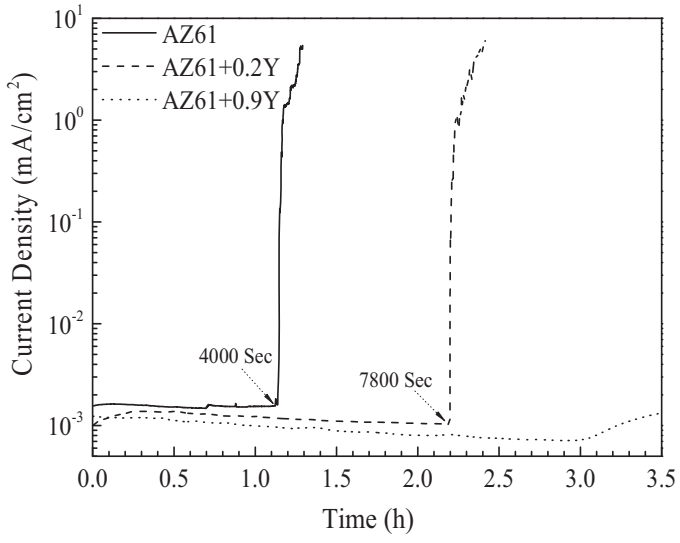

Fig. 5. Current variation with time at the passive potential of −900 $mV_{Ag/AgCl}$.

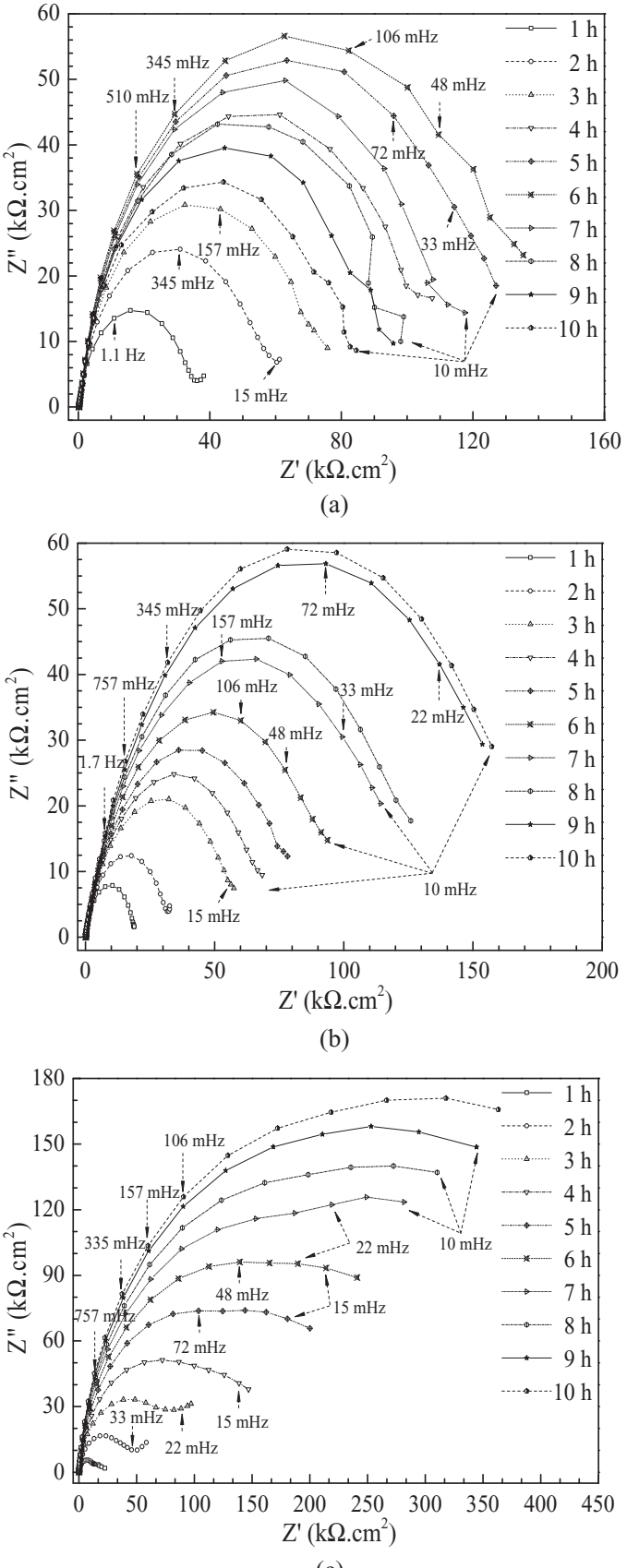

Fig. 6. Nyquist plots of various AZ61 alloys: (a) AZ61, (b) 0.2Y, and (c) 0.9Y addition.

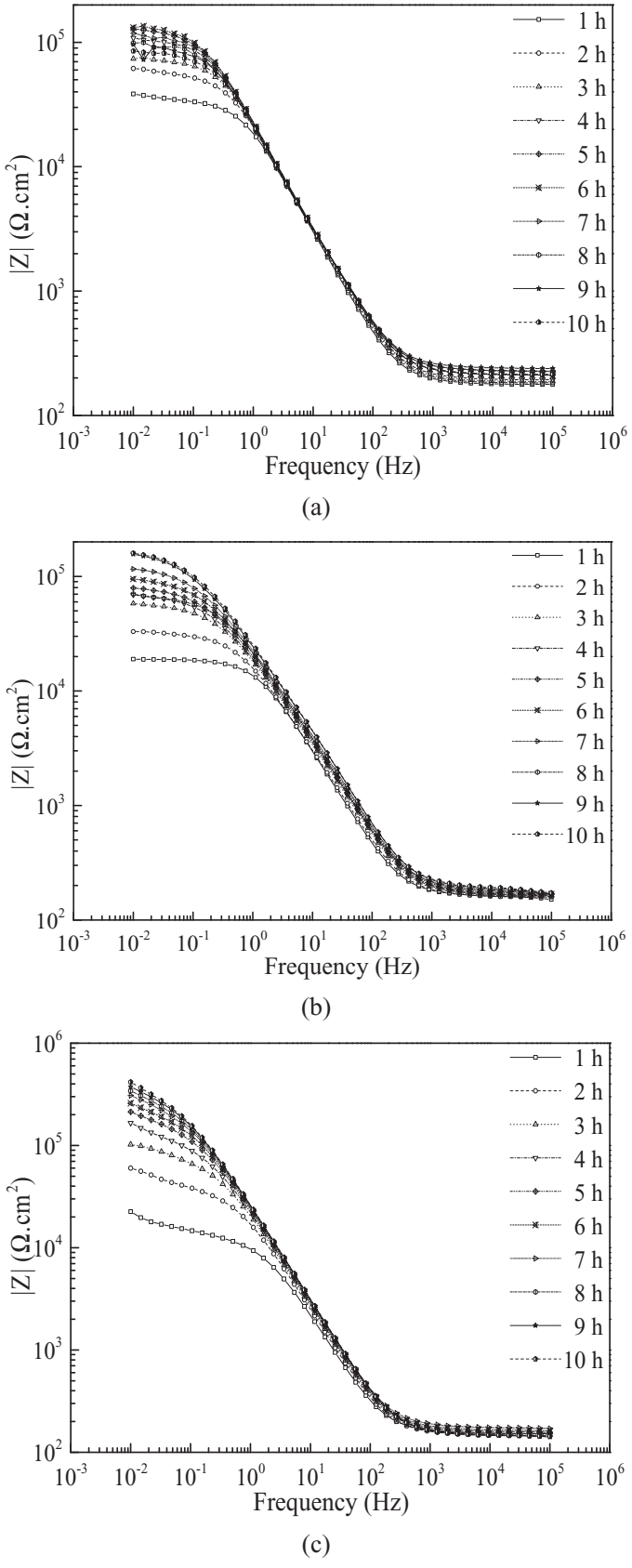

Fig. 7. Bode plots (impedance vs. frequency) of various AZ61 alloys: (a) AZ61, (b) 0.2Y, and (c) 0.9Y addition.

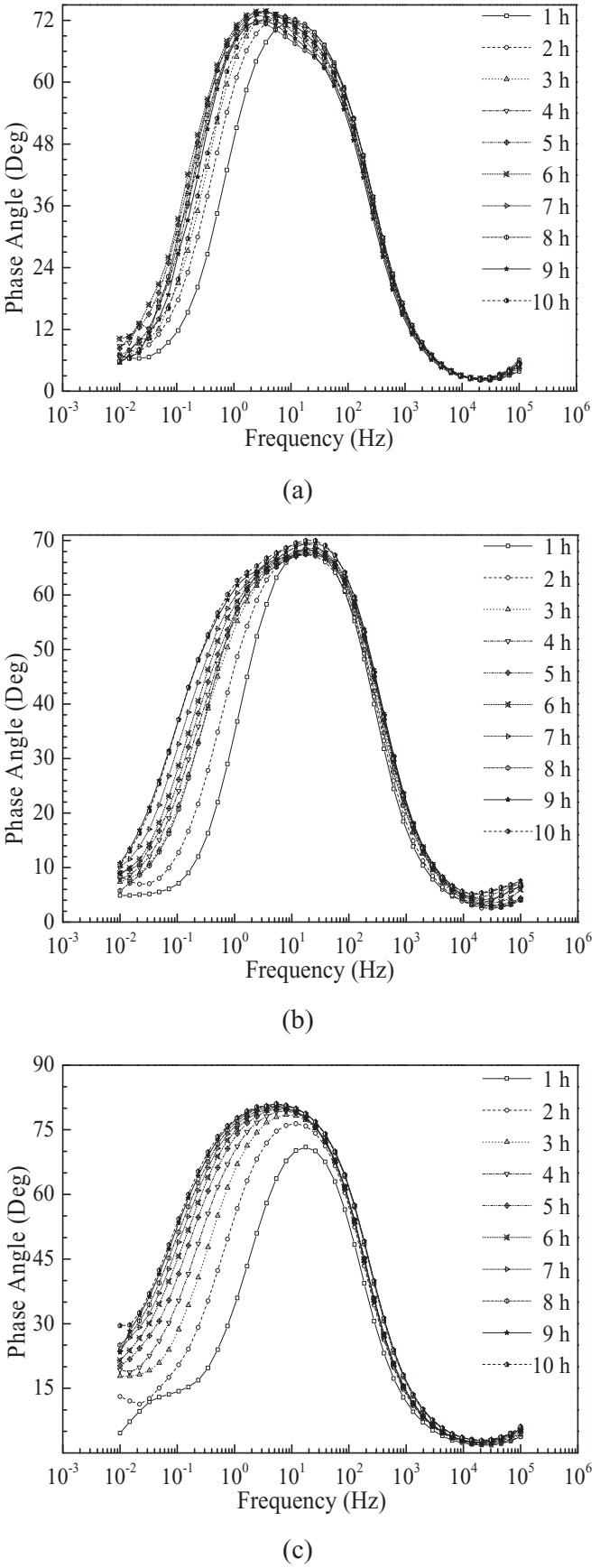

Fig. 8. Bode plots (phase angle vs. frequency) of various AZ61 alloys: (a) AZ61, (b) 0.2Y, and (c) 0.9Y addition.

density and more uniform over the Mg matrix which can act as a barrier.

3.2. Corrosion resistance

Fig. 4a presents the potentiodynamic polarization curves for the alloy electrodes. Based on these curves, the corrosion and pitting potentials were deduced as shown in Fig. 4b. These specimens were passivated at a low passive current density in the investigated solution. In addition, the samples containing Y exhibited lower corrosion potentials and higher pitting potentials, compared to the corresponding potentials for AZ61 specimen. The fact proves that the passive potential and pitting resistance of the AZ61 alloy can be improved by the presence of Y.

Fig. 5 shows the results of potentiostatic test at a constant potential of −900 $mV_{Ag/AgCl}$ for 3.5 hours to study the stability of the passive film. The applied potential was determined from the data in polarization curves in Fig. 4, corresponding to an enrichment of the passive film. It is shown that the current density in all cases was very low and decreased with the increase of Y content, suggesting that there is a very low anodic dissolution of the alloys. However, the current densities increased sharply after 4000 s for AZ61 and 7800 s for AZ61—0.2Y due to the pitting initiation and propagation of pits, whereas the current densities are still stable at low values after 12,600 s for AZ61—0.9Y specimen. Therefore, the results indicate that both pitting resistance and passive stability increase with the increase of Y content, consistent with the results of polarization test shown in Fig. 4.

Fig. 6 shows the Nyquist plots obtained from alloy electrodes after 10 hour immersion in naturally-aerated 0.01 M NaCl solution. Larger impedance values were measured for the Y-containing alloy electrodes (Fig. 6b and c), compared to the AZ61 based alloy. The increase in the diameter of the arc implies an improvement in the charge transfer process. These results prove that the addition of Y content inhabits the corrosion rates of the alloys.

Figs. 7 and 8 show the form of the Bode plots (impedance and phase angle vs. frequency) during immersions for 10 hours at E_{corr}. The high spectra detect the local surface defects, whereas the medium and low frequency spectra detect the process within the film and the process at the metal/film interface, respectively. It is observed that the impedance value and aperture of phase angles increased with the Y content due to the surface film formation. In case of AZ61 specimen, the impedance and aperture of the phase angles were decreased due to the pitting. These results also illustrate that the Y addition promotes the passive film formation.

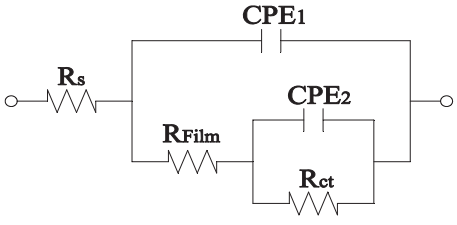

Fig. 9. Equivalent circuit model for fitting EIS data.

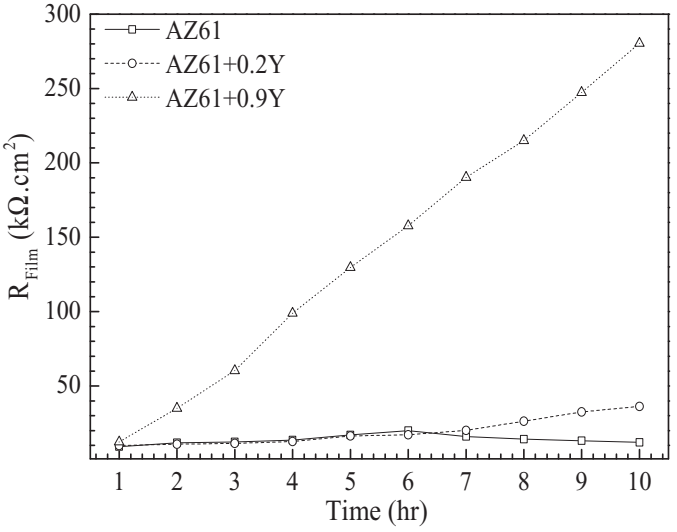

(a)

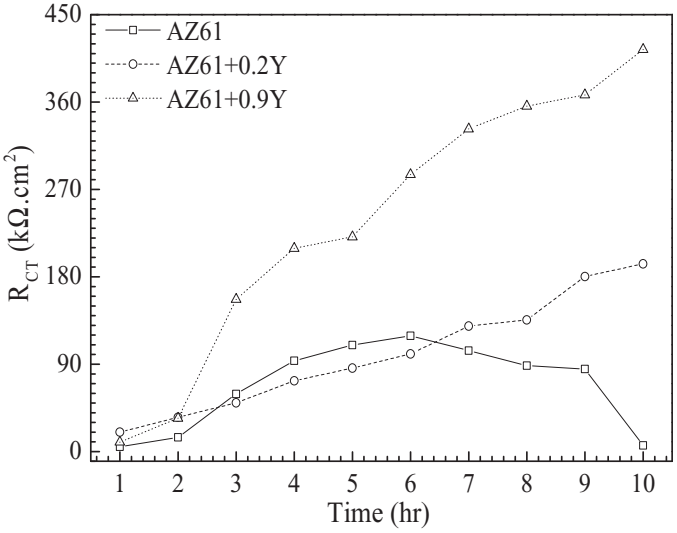

(b)

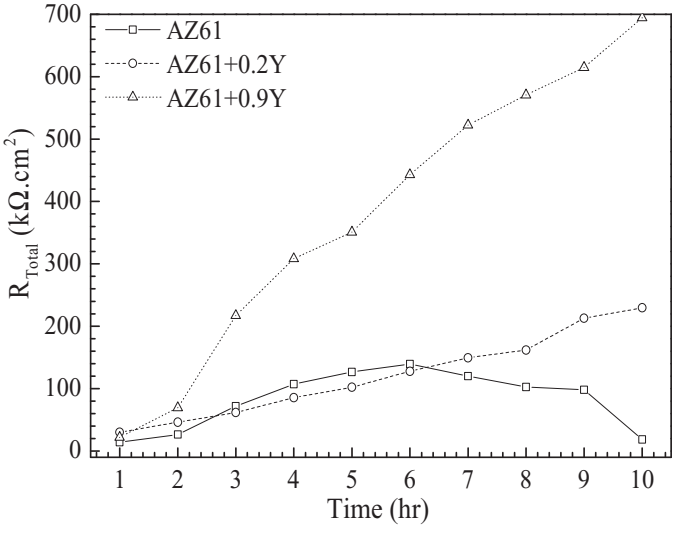

(c)

Fig. 10. Effect of Y content on: (a) film, (b) charge transfer and (c) total resistances.

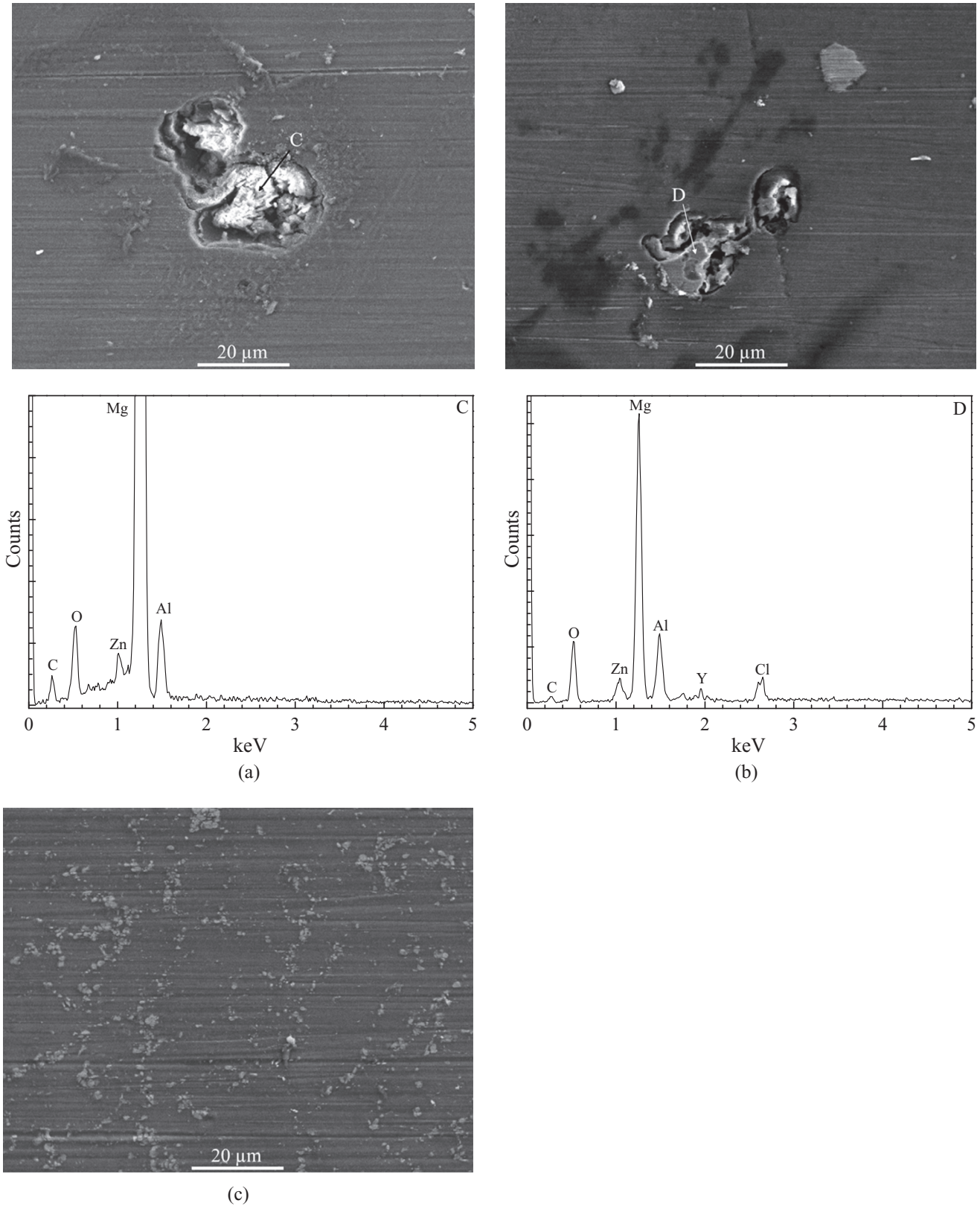

Fig. 11. SEM image and EDS spectrum of the (Al, Zn, and Y)-rich intermetallic particles after pitting initiation: (a) AZ61, (b) AZ61 + 0.2Y, and (c) AZ61 + 0.9Y.

Further information about the electrochemical processes occurring at the solution–electrode interface can be obtained by detailed analysis of impedance spectra using suitable designed equivalent circuits. Fig. 9 represents the equivalent circuits used for fitting EIS data, where R_s stands for the solution resistance, CPE for the constant phase element, R_{film} for the film resistance, and R_{ct} for the charge transfer resistance. The high- (R_{film}) and low- (R_{ct}) frequency resistance components were influenced by

the alloying element. In this case, the capacitor was substituted with a CPE to improve the fitting quality, where the CPE contained a double-layer capacitance (C) and phenomenological coefficient (n). The meaning of n value for a CPE can be referred to our previous study [17]. In the present study, n was consistently maintained near 0.8, showing the deviation from ideal dielectric behavior. Furthermore, n seems to be related to the non-uniform distribution of current caused by roughness and surface defects. The fact illustrates the degree of "non-ideality" of the double layer capacitance, or the extent of the depression of the semicircles in the Nyquist plots.

The Zsimpwin program was adopted to fit the EIS data in order to determine the optimized values for the film and charge transfer resistance parameters (R_{film} and R_{ct}). Fig. 10a illustrates the variation of the passive film resistance (R_{film}) with the immersion time for AZ61—xY. It can be observed that the resistance of the passive film increases steadily with the immersion time during the initial 6 hours and then decreases, while the film resistance increases steadily with the immersion time and Y addition. It suggests that the increase of the Y content improves not only the film resistance but also its stability. Fig. 10b and c shows that the charge transfer and total resistances also increase with the immersion time and the amount of Y addition, exhibiting good corrosion resistance.

4. Discussions

Fig. 11 shows SEM/EDS images for surface morphology after pitting initiation under $-900\ mV_{Ag/AgCl}$ application. No pitting was identified for the 0.9 Y specimen, whereas there was obvious pitting corrosion on the 0.2 wt.% Y and AZ61-based alloy specimens as shown in Fig. 11a and b. The initial pitting shown in Fig. 11a shows that corrosion was serious and a large number of hydrogen bubbles were evolved from an enlarged pit, which developed slowly in Fig. 11b. The summary view of these results shows that the stability of the passive film increases with the addition of Y. Furthermore, the galvanic attack of the AZ61 alloy surface adjacent to the impurities was observed. It also shows that the particle acts as a cathode with respect to matrix, which forms galvanic couples. The EDS spectra obtained from the particle A on the sample surface is shown in Fig. 11a and revealed that the white particles are the Al-containing phases in AZ61 alloy, while Al- and Y-containing phases are observed in AZ61—0.2Y alloy.

From the results of SEM and EDS analyses, the existence of Al-containing phases at the surface was confirmed. These Al-containing phases play a significant role in pit initiation or pit propagation on AZ61-based and AZ61—0.2Y alloys. This is the good evidence that the pitting corrosion was concentrated around Al- and Y-containing phases due to the micro-galvanic corrosion between these phases and the Mg matrix. Thus, in case of AZ61, the Al-containing phases are the major cause for pitting corrosion and also very consistent with reports anywhere. Increasing yttrium content reduces the size of α-grain and alters the distribution of the β-phase ($Mg_{17}Al_{12}$) from continuous network morphology to small and dispersive distribution. It forms secondary intermetallic phase $Al_{11}Y_3$ which has high melting point along the grain boundary. The corrosion resistance of Mg—6Al—1Zn magnesium alloy improved with addition of yttrium. It was confirmed by the results of electrochemical polarization test. Based on the polarization curves, it is seen that fine precipitates of Al—Y intermetallic phase in Mg—6Al—1Zn alloy decrease the corrosion current density, thereby improving the corrosion resistance of the Mg—6Al—1Zn magnesium alloy. Therefore, the improved pitting corrosion resistance as increasing Y addition was related to the finer grain size, higher precipitation density and more uniform over the Mg matrix.

5. Conclusions

The variation of the microstructure is mainly caused by the addition of yttrium which refines the precipitates and matrix grains. The precipitation of the Mg—Al—Zn phase was suppressed by the high density of Mg—(Al, Zn, and Y) compounds in the Y-containing alloy. A higher density and more uniform precipitation with finer α-Mg grains strongly affect the corrosion resistance. Potentiodynamic polarization results show that the pitting potential increases with the Y content, resulting in improved pitting resistance which is consistent with higher film and charge transfer resistances obtained in EIS measurements. Furthermore, the addition of Y reduces the susceptibility to breakdown the passive film due to an increase in the breakdown time of the passive film. SEM/EDS analysis clearly shows that the Al-containing phases are the main cause for pit initiation. The smaller grain size, higher precipitation density and more uniform over the Mg matrix played significant roles in improving stability of the surface film of extruded AZ61 alloy.

References

[1] M. Masoumi, M. Pekguleryuz, Mater. Lett. 71 (2012) 104–107.
[2] G.L. Song, Z. Xu, G.-L. Song (Ed.), Corrosion Prevention of Magnesium Alloys, Woodhead Publishing, 2013, pp. 110–134.
[3] H.S. Kim, W.J. Kim, Corros. Sci. 75 (2013) 228–238.
[4] N.D. Nam, W.C. Kim, J.G. Kim, K.S. Shin, H.C. Jung, J. Alloys Comp. 509 (14) (2011) 4839–4847.
[5] A. Samaniego, I. Llorente, S. Feliu Jr., Corros. Sci. 68 (2013) 66–71.
[6] M. Liu, D. Qiu, M.-C. Zhao, G. Song, A. Atrens, Script. Mater. 58 (5) (2008) 421–424.
[7] G. Galicia, N. Pébère, B. Tribollet, V. Vivier, Corros. Sci. 51 (8) (2009) 1789–1794.
[8] F. Lu, A. Ma, J. Jiang, Y. Guo, D. Yang, D. Song, et al., Corros. Sci. 94 (2015) 171–178.
[9] N. Birbilis, M.A. Easton, A.D. Sudholz, S.M. Zhu, M.A. Gibson, Corros. Sci. 51 (3) (2009) 683–689.
[10] R. Arrabal, B. Mingo, A. Pardo, E. Matykina, M. Mohedano, M.C. Merino, et al., Corros. Sci. 97 (2015) 38–48.
[11] T. Takenaka, T. Ono, Y. Narazaki, Y. Naka, M. Kawakami, Electrochim. Acta 53 (1) (2007) 117–121.
[12] L. Li, X. Zhang, C. Tang, Y. Deng, N. Zhou, Mat. Sci. Eng. A. 527 (4–5) (2010) 1266–1274.
[13] I. Toda-Caraballo, E.I. Galindo-Nava, P.E.J. Rivera-Díaz-del-Castillo, Acta Mater. 75 (2014) 287–296.
[14] A.T.K., J. Mol. Struct. 54 (1979) 307–308.
[15] N. Kashefi, R. Mahmudi, Mater. Des. 39 (2012) 200–210.
[16] H. Schulz, K.H. Thiemann, Solid State Commun. 32 (9) (1979) 783–785.
[17] N.D. Nam, W.C. Kim, J.G. Kim, K.S. Shin, H.C. Jung, Corros. Sci. 51 (12) (2009) 2942–2949.